Click Here for Full Article

A study of the relation between ocean storms and the Earth's hum

Junkee Rhie and Barbara Romanowicz

Berkeley Seismological Laboratory, University of California, Berkeley, 209 McCone Hall, Berkeley, California 94720, USA (rhie@seismo.berkeley.edu; barbara@seismo.berkeley.edu)

[1] We previously showed that the Earth's "hum" is generated primarily in the northern oceans during the northern hemisphere winter and in the southern oceans during the summer. To gain further insight into the process that converts ocean storm energy into elastic energy through coupling of ocean waves with the seafloor, we here investigate a 4-day-long time window in the year 2000 that is free of large earthquakes but contains two large "hum" events. From a comparison of the time functions of two events and their relative arrival times at the two arrays in California and Japan, we infer that the generation of the "hum" events occurs close to shore and comprises three elements: (1) short-period ocean waves interact nonlinearly to produce infragravity waves as the storm reaches the coast of North America; (2) infragravity waves interact with the seafloor locally to generate long-period Rayleigh waves; and (3) some free infragravity wave energy radiates out into the open ocean, propagates across the north Pacific basin, and couples to the seafloor when it reaches distant coasts northeast of Japan. We also compare the yearly fluctuations in the amplitudes observed on the two arrays in the low-frequency "hum" band (specifically at 240 s) and in the microseismic band (2–25 s). During the winter, strong correlation between the amplitude fluctuations in the "hum" and microseismic bands at BDSN is consistent with a common generation mechanism of both types of seismic noise from nonlinear interaction of ocean waves near the west coast of North America.

1. Introduction

[2] Since the discovery of the Earth's "hum" [*Nawa et al.*, 1998], seismologists have tried to determine the source of the continuous background free oscillations observed in low-frequency seismic spectra in the absence of earthquakes.

[3] In the last decade, some key features of these background oscillations have been documented. First, their source needs to be close to the Earth's surface, because the fundamental mode is preferentially excited [*Nawa et al.*, 1998; *Suda et al.*, 1998] and no clear evidence for higher mode excitation has yet been found. Second, these oscillations must be related to atmospheric processes,

because annual [*Nishida et al.*, 2000] and seasonal [*Tanimoto and Um*, 1999; *Ekström*, 2001] variations in their amplitudes have been documented. Finally, they are not related to local atmospheric variations above a given seismic station, since correcting for the local barometric pressure fluctuations brings out the free oscillation signal in the seismic data more strongly [e.g., *Roult and Crawford*, 2000].

[4] Early studies proposed that the "hum" could be due to turbulent atmospheric motions and showed that such a process could explain the corresponding energy level, equivalent to a M 5.8–6.0 earthquake every day [*Tanimoto and Um*, 1999; *Ekström*, 2001]. However, no observations of atmospheric convection at this scale are available to confirm this hypothesis. In the meantime, it was suggested that the oceans could play a role [*Watada and Masters*, 2001; *Rhie and Romanowicz*, 2003; *Tanimoto*, 2003].

[5] Until recently, most studies of the "hum" have considered stacks of low-frequency spectra for days "free" of large earthquakes. In order to gain resolution in time and space and determine whether the sources are distributed uniformly around the globe, as implied by the atmospheric turbulence model [e.g., *Nishida and Kobayashi*, 1999], or else have their origin in the oceans, it is necessary to adopt a time domain, propagating wave approach. In a recent study, using an array stacking method applied to two regional arrays of seismic stations equipped with very broadband STS-1 seismometers [*Wielandt and Streckeisen*, 1982; *Wielandt and Steim*, 1986], we showed that the sources of the "hum" are primarily located in the northern Pacific Ocean and in the southern oceans during the northern hemisphere winter and summer, respectively [*Rhie and Romanowicz*, 2004 (hereafter referred to as RR04)], following the seasonal variations in maximum significant wave heights over the globe, which switch from northern to southern oceans between winter and summer. We suggested that the generation of the hum involved a three stage atmosphere/ocean/seafloor coupling process: (1) conversion of atmospheric storm energy into short-period ocean waves, (2) nonlinear interaction of ocean waves producing longer-period, infragravity waves, and (3) coupling of infragravity waves to the seafloor, through a process involving irregularities in the ocean floor topography. However, the resolution of our study did not allow us to more specifically determine whether the generation of seismic waves occurred

in the middle of ocean basins or close to shore [e.g., *Webb et al.*, 1991; *Webb*, 1998]. The preferential location of the sources of the Earth's "hum" in the oceans has now been confirmed independently [*Nishida and Fukao*, 2004; *Ekström and Ekström*, 2005]. In a recent study, *Tanimoto* [2005] showed that the characteristic shape and level of the low-frequency background noise spectrum could be reproduced if the generation process involved the action of ocean infragravity waves on the ocean floor, and suggested that typically, the area involved in the coupling to the ocean floor need not be larger than about 100×100 km^2. However, the linear process proposed may not be physically plausible, because of the difference in wavelength between infragravity and elastic waves (S. Webb, personal communication, 2006).

[6] On the other hand, oceanographers have long studied the relation between infragravity waves and swell. Early studies have documented strong correlation between their energy levels, which indicate that infragravity waves are driven by swell [e.g., *Munk*, 1949; *Tucker*, 1950]. Theoretical studies have demonstrated that infragravity waves are second order forced waves excited by nonlinear difference frequency interactions of pairs of swell components [*Hasselmann*, 1962; *Longuet-Higgins and Stewart*, 1962]. A question that generated some debate was whether the observed infragravity waves away from the coast are "forced" waves bound to the short carrier ocean surface waves and traveling with their group velocity, or "free" waves released in the surf zone and subsequently reflected from the beach which, under certain conditions, may radiate into deep ocean basins [e.g., *Sutton et al.*, 1965; *Webb et al.*, 1991; *Okihiro et al.*, 1992; *Herbers et al.*, 1994, 1995a, 1995b]. In particular, *Webb et al.* [1991] found that infragravity wave energy observed on the seafloor away from the coast was correlated not with the local swell wave energy but with swell energy averaged over all coastlines within the line of sight of their experimental sites, in the north Atlantic Ocean and off-shore southern California.

[7] Recently, we analyzed the relation between ocean storms off-shore California and infragravity wave noise observed on several broadband seafloor stations in California and Oregon [*Dolenc et al.*, 2005a]. We also found that the seismic noise observed in the infragravity wave band correlates with significant wave height as recorded on regional ocean buoys, and marks the passage of the storms over the buoy which is closest to the shore.
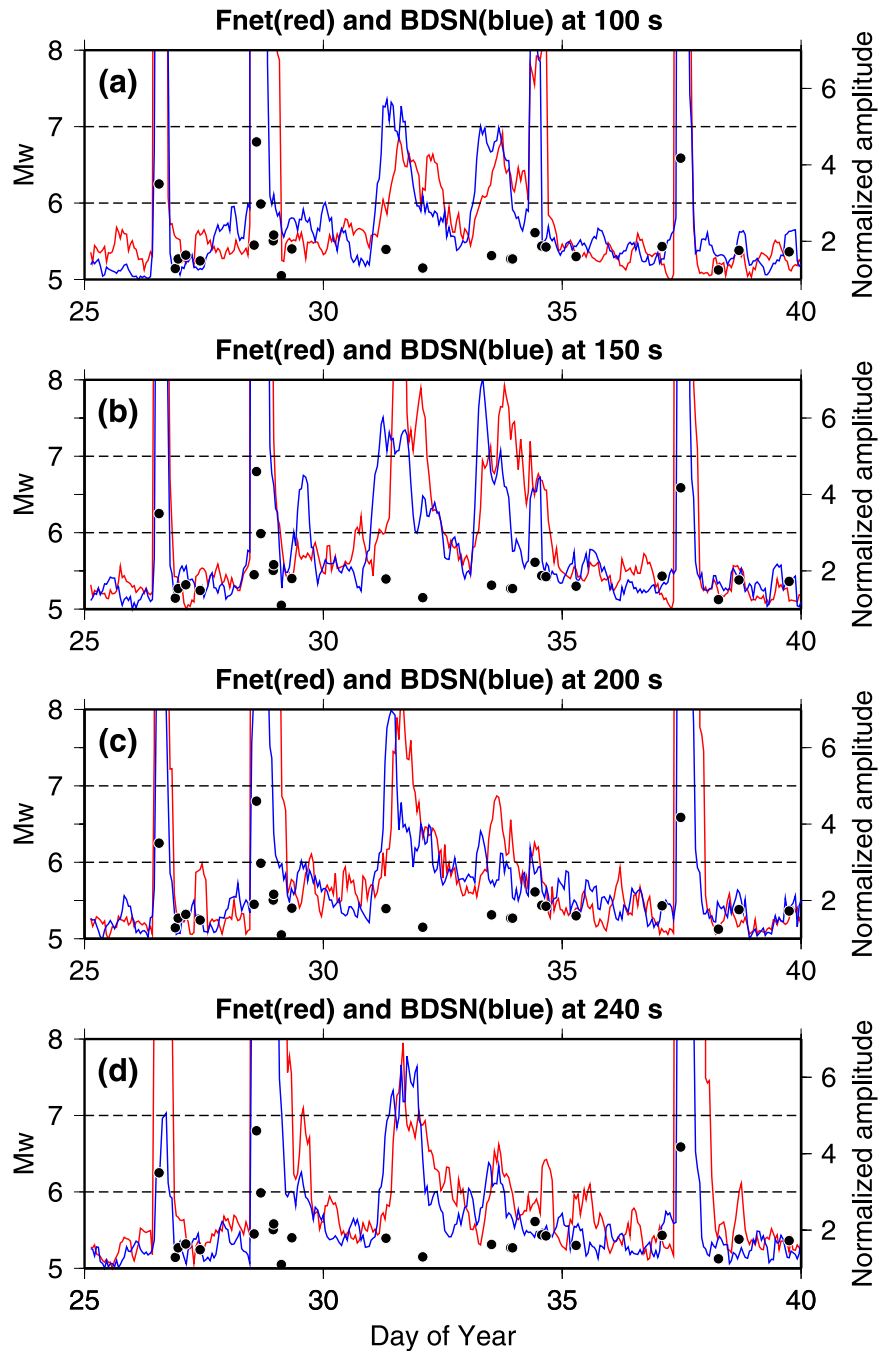
Fnet(red) and BDSN(blue) at 100 s

Fnet(red) and BDSN(blue) at 150 s

Fnet(red) and BDSN(blue) at 200 s

Fnet(red) and BDSN(blue) at 240 s

Figure 1. (a) Maximum stack amplitude (MSA, see definition in text) filtered using a Gaussian filter with center period of 100 s for BDSN (blue) and F-net (red), normalized by minimum value of MSA for a given time window. The linear scale on the y axis to the right is used for the normalized MSA to more clearly see the variations in amplitude of the background noise. Black dots represent earthquakes which occurred during the period considered. The corresponding scale is logarithmic (moment magnitude) and is given on the y axis to the left. (b–d) Same as Figure 1a for 150, 200, and 240 s.

More recent results based on data from an ocean floor station further away from shore [*Dolenc et al.*, 2005b] indicate that the increase in amplitude in the infragravity frequency band (50–200 s) associated with the passage of a storm occurs when the storm reaches the near coastal buoys, and not earlier, when the storm passes over the seismic station. This implies that pressure fluctuations in the ocean during the passage of the storm above the

Table 1. $M_w > 5.0$ Earthquake Catalog From 25 January to 9 February in 2000 From NEIC

Date	Time	Latitude	Longitude	Depth	Mag.
2000/01/25	16:43:22.95	27.6630	92.6310	33.0	5.20
2000/01/26	13:26:50.00	−17.2720	−174.0020	33.00	6.30
2000/01/26	21:37:57.77	30.9730	95.5020	33.00	5.20
2000/01/26	23:00:19.94	40.0210	52.9010	33.00	5.30
2000/01/26	23:34:04.50	−23.7220	−66.4770	221.60	5.00
2000/01/27	02:49:44.91	−34.8070	−105.4590	10.00	5.40
2000/01/27	10:10:57.25	31.6780	141.6860	33.00	5.30
2000/01/28	08:49:30.87	7.4570	−77.8500	21.40	5.40
2000/01/28	13:17:52.87	−7.4850	122.6780	574.90	5.50
2000/01/28	14:21:07.34	43.0460	146.8370	61.10	6.80
2000/01/28	16:39:24.28	26.0760	124.4960	193.90	6.00
2000/01/28	17:57:00.55	14.4350	146.4620	45.20	5.20
2000/01/28	22:42:26.25	−1.3470	89.0830	10.00	5.50
2000/01/28	22:57:51.70	−9.6910	118.7640	83.40	5.60
2000/01/29	02:53:54.89	4.8570	126.2590	100.00	5.10
2000/01/29	05:48:10.77	−20.5630	−178.2880	562.90	5.00
2000/01/29	08:13:10.73	−8.6330	111.1370	60.70	5.40
2000/01/31	07:25:59.74	38.1140	88.6040	33.00	5.40
2000/02/01	00:01:05.42	−4.3580	151.9070	189.00	5.20
2000/02/01	02:00:10.68	13.0100	−88.8470	55.00	5.20
2000/02/02	12:25:21.92	−49.0240	124.9790	10.00	5.40
2000/02/02	21:58:49.71	−5.7300	148.9320	112.80	5.30
2000/02/02	22:58:01.55	35.2880	58.2180	33.00	5.30
2000/02/03	10:24:57.77	65.0087	−154.2390	10.00	5.98
2000/02/03	13:42:25.04	13.5720	121.5460	33.00	5.50
2000/02/03	15:53:12.96	75.2710	10.1950	10.00	5.50
2000/02/04	07:02:11.39	−40.6310	−85.9180	10.00	5.30
2000/01/25	16:43:22.95	27.6630	92.6310	33.0	5.20
2000/02/06	02:08:07.14	1.2950	126.2720	33.00	5.50
2000/02/06	11:33:52.28	−5.8440	150.8760	33.00	6.60
2000/02/07	06:34:49.67	43.3680	147.4330	61.50	5.20
2000/02/07	16:41:04.58	31.0370	141.6940	33.00	5.40
2000/02/08	18:01:27.18	−21.9360	170.0680	33.00	5.40
2000/02/09	04:28:00.48	−16.6660	−172.6960	33.00	5.20
2000/02/09	09:33:54.05	−30.1050	−178.1130	56.70	5.00
2000/02/09	18:40:37.83	−27.6220	65.7240	10.00	5.10

station can be ruled out as the direct cause of the low-frequency seismic noise.

[8] In this paper, we investigate these processes further in an attempt to better understand where the coupling between infragravity waves and ocean floor occurs, generating the seismic "hum." In particular, we describe in detail observations made during one particular time period of unusually high levels of low-frequency noise. We also present comparisons of the observed low-frequency seismic "hum" with noise in the microseismic frequency band (2–25 s), and discuss the relation between the two phenomena.

2. Earthquake "Free" Interval 2000.031−034

[9] In our previous study [RR04], we extracted time intervals which were not contaminated by earthquakes, using strict selection criteria based on event magnitude. This significantly limited the number of usable days in a given year. For example, only 64 days of "earthquake free" data were kept for the year 2000. Among these, we identified the time interval 2000.030 to 2000.034 (i.e., 30 January to 3 February) as a particularly long interval free of large earthquakes, during which the background noise amplitude was unusually high, and during which two large noise events were observed, that could be studied in more detail.

[10] As described in RR04, we considered data at two regional arrays of very broadband seismometers, BDSN (Berkeley Digital Seismic Network) in California, and F-net in Japan. For each array, we stacked narrow-band filtered time domain vertical component seismograms according to the dispersion and attenuation of Rayleigh waves, assuming plane wave propagation from an arbitrary azimuth. Here, we apply a 6 hour running average with a
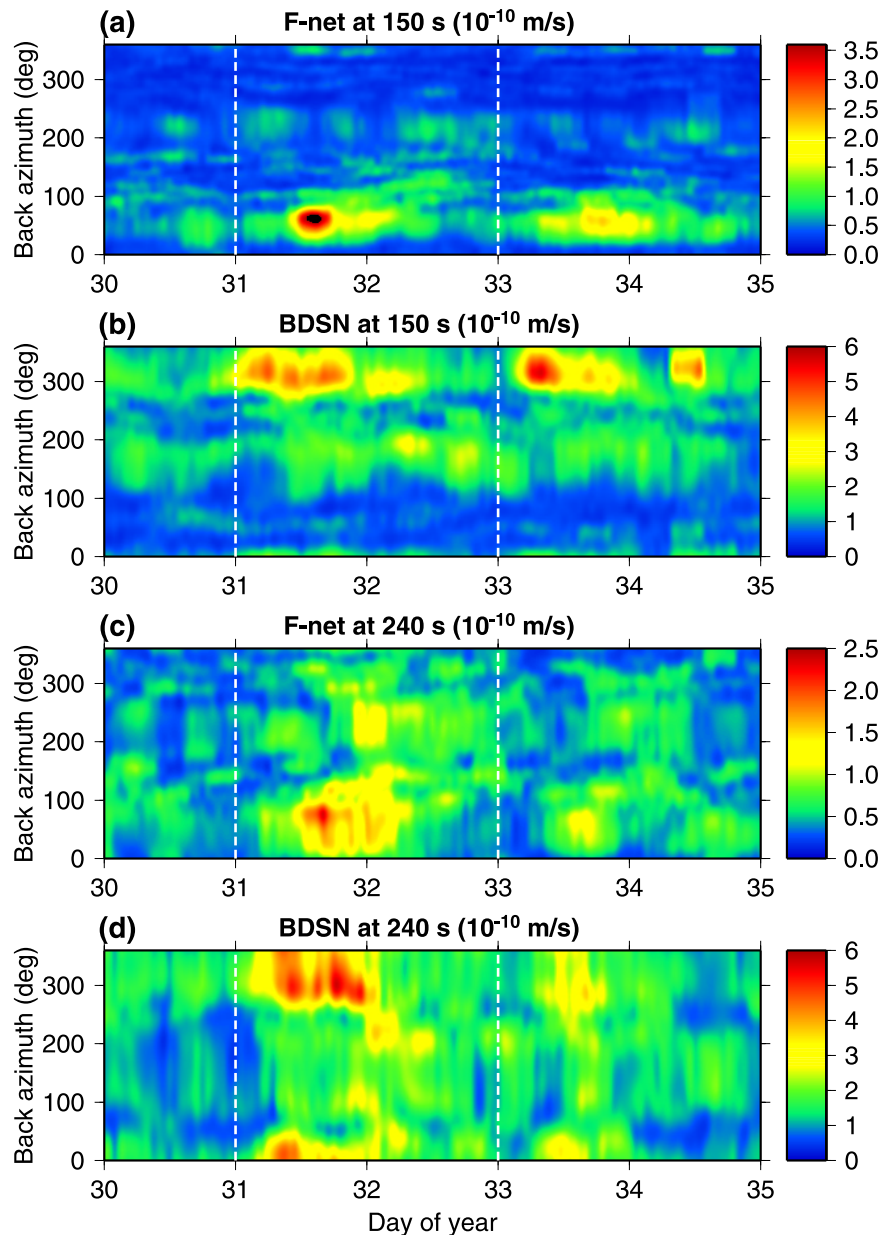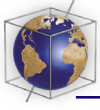
Figure 2. (a) Mean stack amplitude averaged over 6 hour sliding window (window shifted 1 hour between resolutions) as a function of time and back azimuth for F-net. A Gaussian filter with center period of 150 s was applied before stacking. (b) Same as Figure 2a for BDSN. (c) Same as Figure 2a for center period of 240 s. (d) Same as Figure 2c for BDSN. The time difference between corresponding energy arrivals at the two arrays on day 31 is about 8–10 hours, with F-net lagging behind BDSN. This is more clearly seen in the shorter-period plot.

time step of 1 hour to the stacked data at BDSN and F-net respectively. At each time step, the stack amplitude has a maximum corresponding to a particular back-azimuth. We consider the resulting maximum stack amplitudes (MSA) as a function of time. We show in Appendix A that the level of the background "hum" is consistent with previous estimates [e.g., *Tanimoto and Um*, 1999; *Ekström*, 2001].

[11] We consider the 15 day period 2000.25 to 2000.40. In Figure 1, we plot the MSA as a function of time in four different period bands. We here use a linear scale for the MSA (different from Figure A1) to more clearly see the variations in amplitude of the background noise. We note the well defined signature of large earthquakes, which have a sharp onset, a slower decay and a relatively sharp end. At the time resolution considered here, this onset is practically coincident at both arrays.
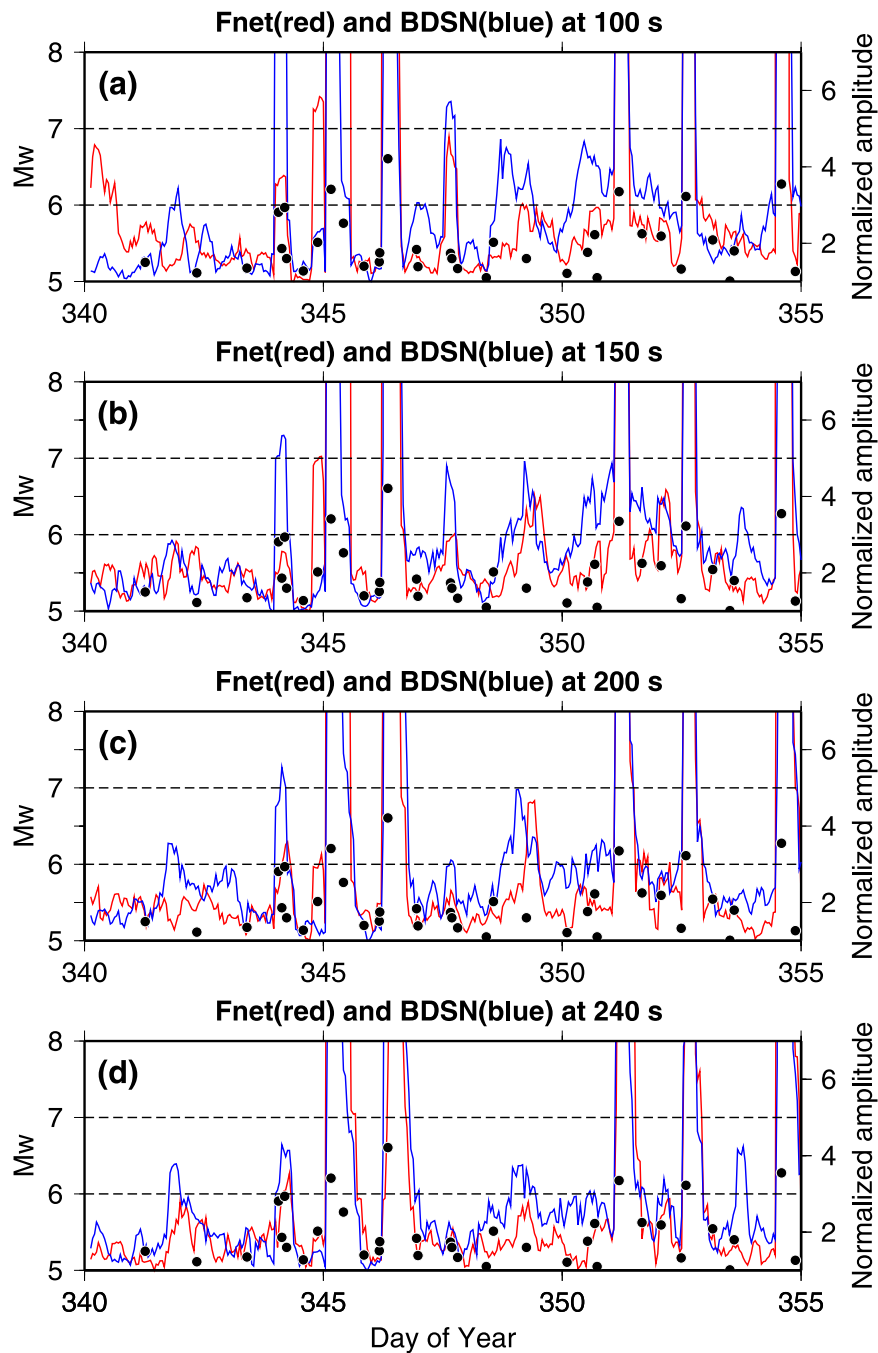
Figure 3. Same as Figure 1 for days from 340 to 355 in 2002.

The duration of the earthquake signal increases with the size of the earthquake and is typically on the order of 0.5 day for M_w 6 and 1–1.5 day for M_w 7 earthquakes, after which the signal drops below the average background noise level. This is consistent with what one expects from the decay of Earth circling mantle Rayleigh waves generated by large earthquakes.

[12] Table 1 lists all earthquakes larger than M 5.0 during these 15 days, as reported in the NEIC catalog. During the time interval 2000.031 to 2000.034, there are no earthquakes larger than M 5.5, yet the background noise rises well above the noise floor, forming two particularly long events, with a very different signature from that of earthquakes: the rise time is longer, the decay very slow and the ratio of the duration of each event to its maximum amplitude, significantly larger. These two noise events are observed on both arrays (i.e., in California and in Japan), and there is a lag time of
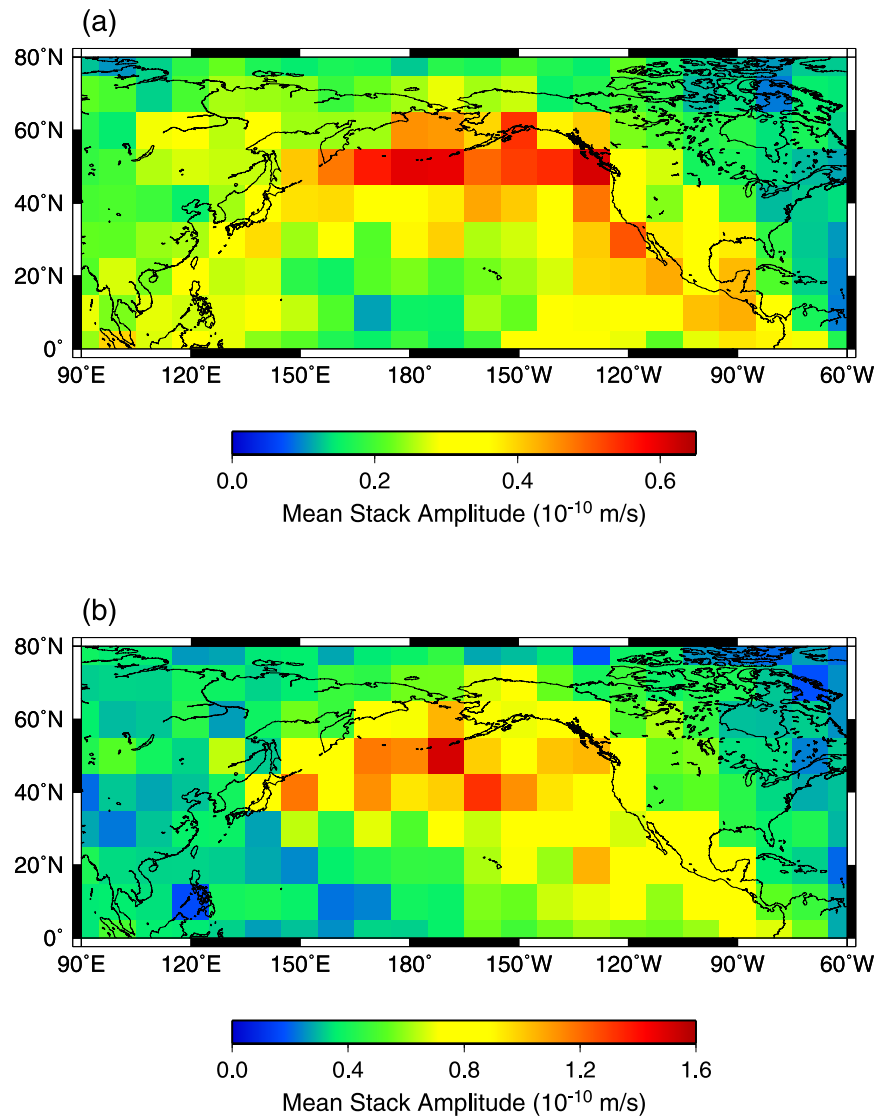
(a)

(b)

Figure 4. (a) Results of grid search method to locate the source of continuous long-period Rayleigh waves on 31 January 2000. Six hour waveforms Gaussian filtered with center period of 100 s from F-net, BDSN, and 10 European stations are used. Color indicates the mean stack amplitude over a 6 hour time window (2000.031,14:00–2000.031,20:00 UTC) after correcting waveforms at individual stations for attenuation and dispersion. (b) Same as Figure 4a for 150 s.

several hours between the two arrays. The second event is weaker at the longest periods. We verify that the back-azimuth corresponding to the maximum amplitude is very stable during these two events, as illustrated in Figure 2, which also emphasizes the delay of about 8–10 hours between the main energy arrivals at BDSN and F-net. We will discuss these events in detail in what follows.

[13] This particular "earthquake free window" is unique in that it lasts several days, and the noise events are large. However, noise events with similar characteristics are observed at other times as

well. For example, Figure 3 shows a similar plot for the time period 2002.340 to 2002.355, in which we observe a noise event beginning on day 2002.349, showing similar time evolution as for the events in 2000 described above: a slow rise time and lag of ~8–10 hours between the two arrays. It is followed by a second noise event of similar characteristics, but partially hidden behind an earthquake of $M_w > 6$. In what follows, we return to the time period 2000.031–034 for further analysis.
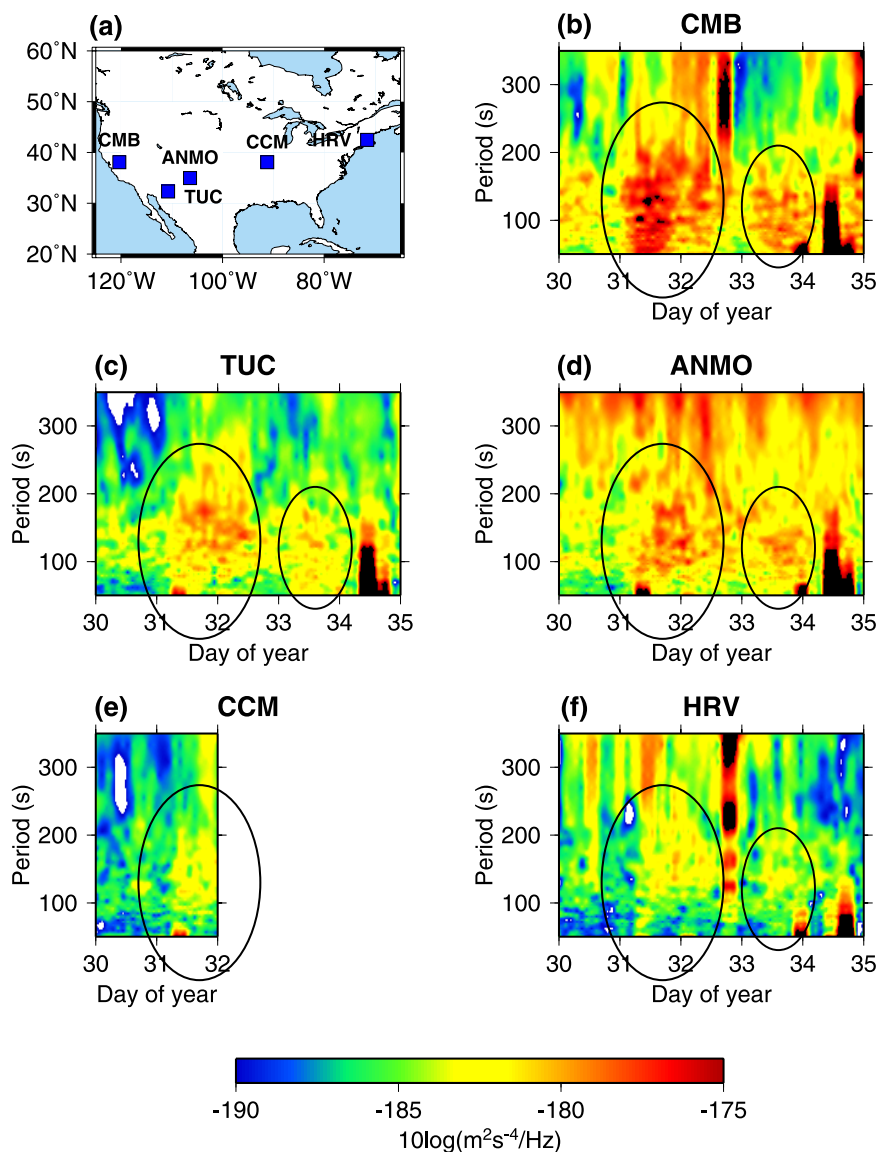
Figure 5. (a) Locations of five quiet seismic stations in North America. (b) Power spectral density (PSD) at CMB. It is clear that two large seismic energy arrivals (highlighted with black circles) are present on days 031 and 033. (c–f) Same as Figure 5b for TUC, ANMO, CCM, and HRV, respectively. For CCM the data are missing after day 33 through day 35. Large amplitude signals for periods <120 s on days 34 and 35 correspond to earthquakes (see Table 1).

[14] The large noise events observed on days 2000.031 and 2000.033 after applying a smoothing moving average to the MSA, are the coalescence of multiple smaller events, which, as we showed previously, propagate across the two arrays with the dispersion characteristics of Rayleigh waves (see Figure 1 in RR04). In order to locate the sources of these disturbances in RR04, we applied a back-projection grid-search method to the original time series, after band-pass filtering between 150–500 s, over a 6 hour period containing the maximum stack amplitude on day 2000.031. We showed that the sources of Rayleigh waves that

best fit the amplitudes observed both at BDSN and F-net are located in the North Pacific Ocean basin. We here apply the same back-projection method, but using a narrow band filter centered at 150 and 100 s respectively, and obtain a band of source locations which follows the north Pacific shoreline, as illustrated in Figure 4. This is particularly clear at 100 s.

[15] In order to obtain a stable solution using the grid search method, it is necessary to process a time interval of length about 6 hours, indicating that many of the small events which compose the
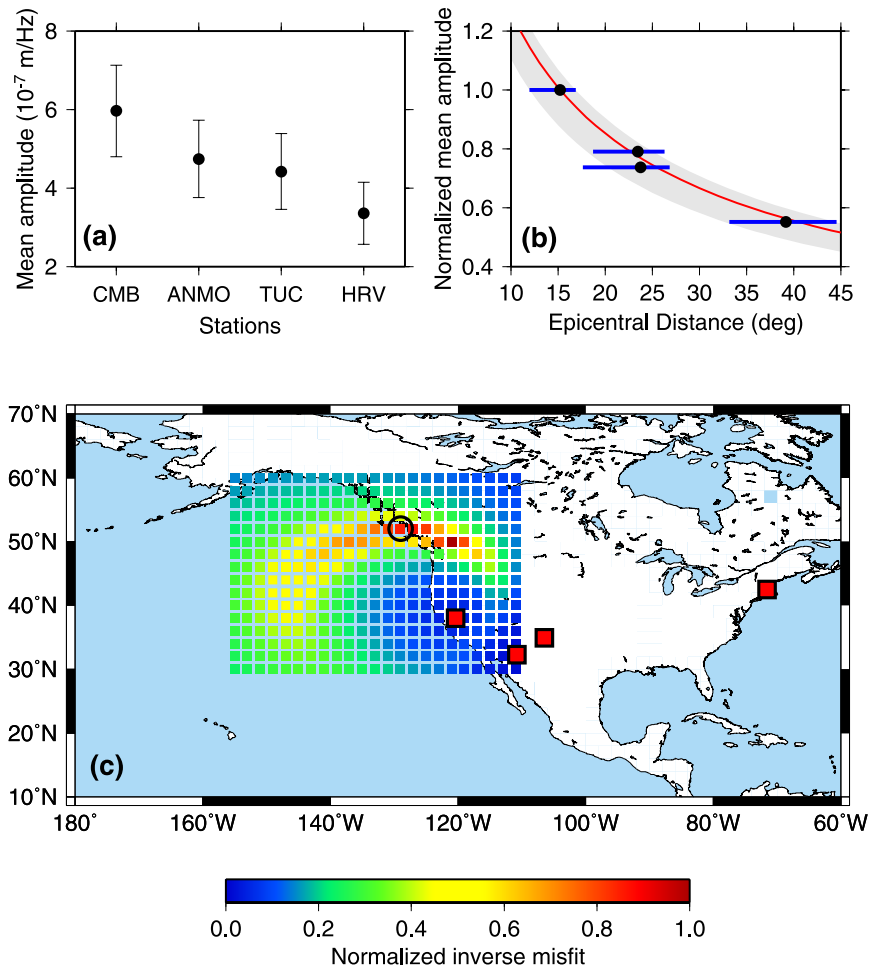
Figure 6. (a) Mean amplitude estimates and corresponding errors at stations considered in Figure 5. Error is estimated by random perturbation of time (±6 hour) and period (±30 s) window used for averaging. (b) Normalized observed mean amplitudes (black dots) and the theoretical attenuation curve (red) for the seismic source location indicated by a circle in Figure 6c. Gray shaded region and horizontal blue bars indicate the possible range of theoretical attenuation curves and epicenters from stations to possible source locations giving the good fit (i.e., normalized inverse misfit >0.7). (c) Results of grid search for the location of the source of PSD noise highlighted in Figure 5. The PSD amplitudes were corrected for attenuation and geometrical spreading. The color scale represents the normalized inverse of the misfit between observed and predicted amplitudes (this way, the minimum misfit is always equal to 1). The circle indicates the off-shore location with small misfit.

larger noise event on day 2000.031 are too small to be studied individually, at least with this method: the minimum duration of the time window necessary to obtain a stable result is controlled by the available signal/noise ratio in the stacks. Here we show that the large "composite" event, obtained when using the 6 hour moving average, propagates west to east across the whole North American continent, with an amplitude decay consistent with the propagation of Rayleigh waves. Instead of stacking the noise data over an array of broadband seismic stations, we here consider five quiet broadband stations in North America, and, for each of them, we compute power spectral density

(PSD) as a function of time, with a 6 hour moving window and a 1 hour lag (Figure 5). All five stations show an increase in background noise during days 31–32, and another one, with smaller amplitude and narrower frequency range, on day 33 (except for CCM for which data are not available on that day). Figure 6a compares the mean Fourier amplitudes at stations CMB, TUC, ANMO and HRV, averaged over the period range 100–200 s and time range 2000.31,00:00 and 2000.32,06:00. We chose this period range, because at lower frequencies, the background noise is dominated by site effects at some of the stations. From the amplitude decay it is possible to obtain a very rough
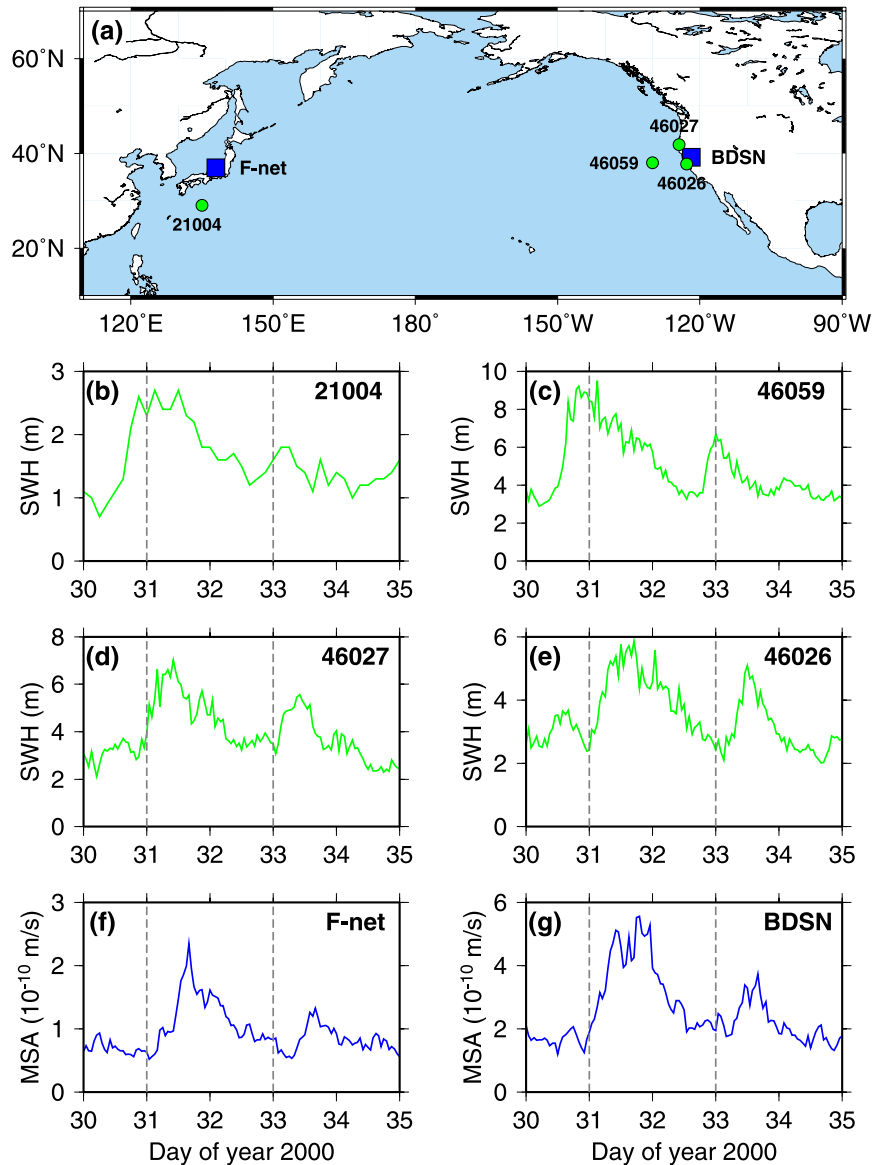
Figure 7. (a) Location of the two seismic arrays (blue squares) and ocean buoys (green dots). (b) Significant wave height recorded at buoy 21004. (c–e) Same as Figure 7b for buoys 44059, 46027, and 46026. (f) Maximum stack amplitude (MSA) Gaussian filtered with center period of 240 s recorded at F-net. (g) Same as Figure 7f for BDSN. Peaks in ocean wave data at off-shore buoys (21004 and 46059) arrive earlier than seismic peaks. For BDSN, arrival times of seismic energy are closer to those of the ocean wave peaks at buoys near the coast (46027 and 46026). The events arrive latest on F-net. Note that the MSA is also lower at F-net than at BDSN, consistent with more distant sources.

estimate of the location of the source of Rayleigh waves by forward amplitude modeling. The results are shown in Figure 6c, using CMB, TUC, ANMO and HRV. Because the available azimuth range is not very wide, there is a large uncertainty in the longitude of the inferred source. However, it is compatible with a location near the west coast of North America. Figure 6b compares the observed and predicted average Fourier amplitudes at four stations. The amplitudes are normalized to those of

the most western station (CMB) and the predicted amplitudes are computed assuming the Q model of PREM for Rayleigh waves [*Dziewonski and Anderson*, 1981] and accounting for geometric spreading.

3. Correlation With Ocean Buoy Data

[16] To further investigate the origin of the noise events on days 2000.031 and 2000.033, we now

(a) 2000.031,00(hh)

(b) 2000.031,06(hh)

(c) 2000.031,12(hh)

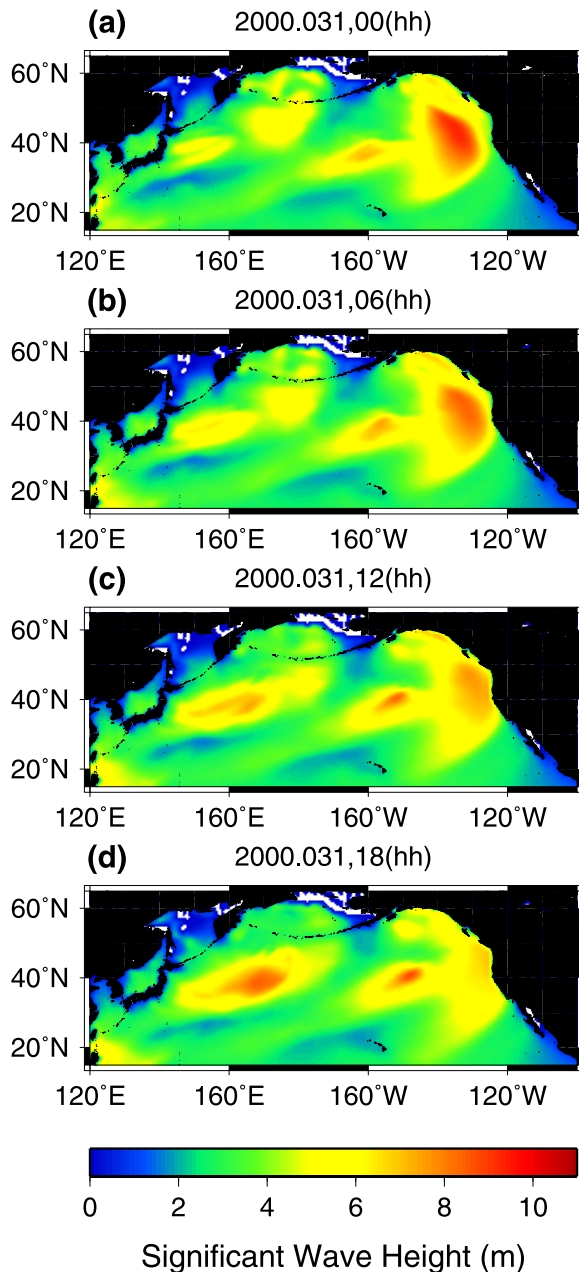**(d)** 2000.031,18(hh)

Significant Wave Height (m)

Figure 8. Significant wave height map on 31 January 2000 for the north Pacific Ocean, based on WAVEWATCH III. (a–d) Different time windows from 0 to 18 hour with 6 hour interval.

turn to a comparison with ocean buoy data. We collected significant wave height (SWH) data measured at buoys deployed in the north Pacific by the National Ocean and Atmospheric Administration (NOAA) and the Japan Meteorological Agency (JMA) and operational during those days. We compare SWH time series for this time period to the time evolution of the maximum stack amplitudes at BDSN and F-net for the same time interval. Figure 7 shows such a comparison for buoys located near Japan and near the California coast. The time series on all buoys closely resemble the "source signature" on the seismic stacks, shown here at a period of 240 s. This is the case for the event on 2000.031 as well as for the smaller one on 2000.033. The seismic noise events on BDSN lag those observed on buoy 46059 by about 10–12 hours, but are more or less coincident (to within 1 hour, which is the minimum resolution of these plots) with the events observed on the near shore buoys, indicating that the location of the coupling between ocean waves and the seafloor occurs somewhere between buoy 46059 and the shore, which is consistent with the results of Figure 6c. The ocean storm which generated the short-period waves observed on buoys both near Japan and near the western US moved from east to west across the north Pacific basin. Unfortunately, we could not find any buoy data closer to the eastern coast of Japan, or in other parts of the western Pacific Ocean. To further investigate the source of these waves, we therefore turn to wave models. Figure 8 shows snapshots of the evolution of wave height in the northern Pacific for day 2000.031, from the WAVEWATCH III model [*Tolman*, 1999]. During that day, a large storm arrives from the west toward the coast of California and Oregon. It reaches the coast, according to the model, between 6h and 12h on day 2000.031. It is followed by a smaller "tail," about 3000 km behind, which, in turn, according to the WAVEWATCH III model, reaches the coast between 0h and 6h on day 2000.033 (not shown). The following storm system, which forms in the western part of the north Pacific (around longitude 160°E on Figure 8) on day 2000.031 develops into a stronger storm over the next few days. This can be seen in the animation provided by NOAA at http://ursus-marinus.ncep.noaa.gov/history/waves/nww3.hs.anim.200001.gif and http://ursus-marinus.ncep.noaa.gov/history/waves/nww3.hs.anim.200002.gif. This storm is not associated with any significantly increased seismic noise on BDSN or F-net (Figure 1). Notably however, in contrast to the previous one, this storm does not reach the California coast, but dissipates in the middle of the ocean. The distribution of wave heights on Figure 8, together with the observation of the significant delay in the stack energy at F-net with respect to the BDSN (see also Figure 2), leads us to propose the following sequence of events.

[17] On day 2000.031, a large storm, which developed two days earlier in the middle of the north
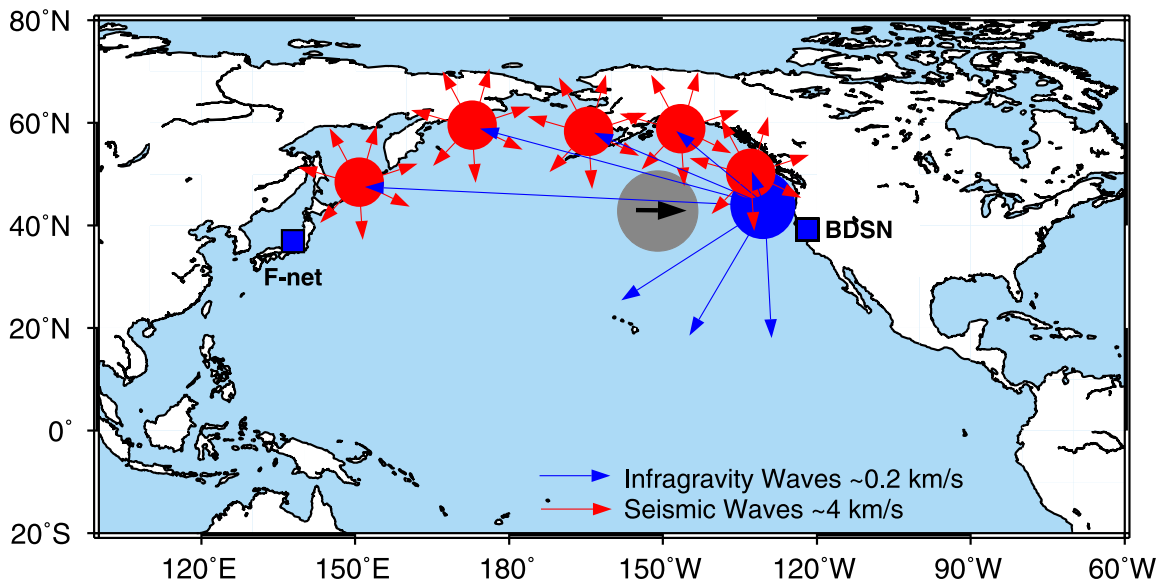
Figure 9. A schematic plot of the mechanism of conversion of energy from storm-related ocean surface waves to seismic waves. Gray circle indicates the moving storm, and blue and red circles (arrows) represent the source regions (radiation) of infragravity and seismic waves, respectively.

Pacific basin (according to wave models and buoy data) and moving eastward toward North America, reaches the vicinity of the western United States coast. A second storm, weaker, but with similar characteristics, follows by about 2 days. The seismic background noise observed on the BDSN and F-net arrays has the same amplitude signature, as a function of time, as the storms. The process that converts the storm energy into seismic energy, which then propagates as Rayleigh waves, in particular through the North American continent, appears to involve several steps (Figure 9): when the storm approaches the US coast with its rough seafloor topography, short-period ocean waves interact nonlinearly to produce infragravity waves. Part of the infragravity wave energy then converts to seismic waves locally, to produce the background noise event observed on BDSN, and part is reflected back out to the ocean and travels across the Pacific basin, in agreement with oceanographic studies of the generation of infragravity waves [e.g., *Munk et al.*, 1964; *Elgar et al.*, 1992; *Herbers et al.*, 1995a, 1995b]. We estimate that, at ~220 m/s, "free" infragravity waves propagate about 6000–8000 km in 8–10 hours. Consistent with the back-azimuth of the maximum arrival of energy, the conversion from infragravity waves to seismic waves detected on F-net primarily occurs in the vicinity of the western Aleutian arc. We note that the absolute level of MSA is larger at BDSN than at F-net (e.g., Figures 2 and 7), in agreement with the

inference that the source for F-net should be comparatively more distant and also weaker.

[18] We infer that free infragravity waves play a role in generating the seismic disturbances in Japan because of the 8–10 hour time delay between stack maxima on BDSN and F-net. This is consistent with observations of remotely generated infragravity waves [e.g., *Herbers et al.*, 1995a]. This time delay is too short for propagation of short-period ocean waves (and also "bound" infragravity waves) from the center of the north Pacific basin, and much too long for propagation of seismic waves from a source near the US coast to Japan. An alternative scenario for the sources of seismic noise on F-net could involve the storm which forms on the Japan side of the Pacific in the middle of day 2000.031 (Figure 8). However, we rule this out, because this storm intensifies only later and reaches its peak around 03h on day 2000.032, which is much later than the long-period seismic peak on F-net.

[19] We note that the generation of large infragravity waves from short-period ocean waves along the east coast of the pacific (Canada, US) rather than the west coast (Japan) is due to the fact that prevailing winds are westerlies, and therefore most ocean waves are driven from the west to the east, interacting nonlinearly only with the coasts on the east side of ocean basins.
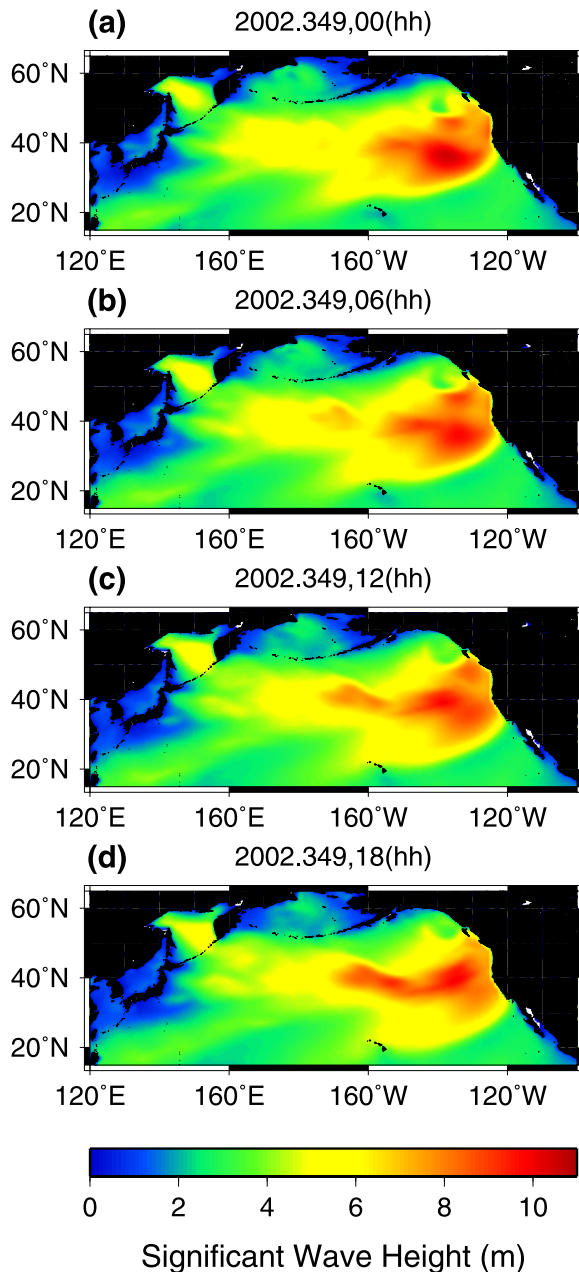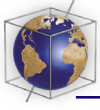
Figure 10. Significant wave height map on 15 December 2002 based on WAVEWATCH III. (a–d) Different time windows from 0 to 18 hour with 6 hour interval.

[20] In summary, the seismic sources that form the composite events on days 2000.031 and 2000.033 are distributed around the Pacific, both in time and space, but have a common cause: a strong storm system which "hits" the North American coast broadside. A similar type of storm which reaches North America from the west, occurs on day 2002.349 (Figure 10), causing the disturbances observed on Figure 3. We infer that the efficiency

of generation of seismic waves is particularly high for these storms, due to their direction of approach to the North American coast, and the fact that these storms actually reach the coast. This is why we can observe these remarkable "noise events" on the stacks at BDSN and F-net so clearly. We have evidence of directionality of the process, in that station COL (Alaska) does not show any increase of seismic noise in the 70–250 s pass band during the same time period. At least, it is below detection level by our methodology involving PSD spectra, even though there is an indication, from the noise in the microseismic bandpass (2–25 s) of a storm reaching the Alaska coast nearby at the end of day 2000.031 (Figure 11). Such directionality would also explain why we can so clearly follow the particular seismic disturbance on day 2000.031 across North America.

[21] Other north Pacific storms must also generate long-period seismic noise, however, the corresponding noise "events" cannot often be identified as clearly because they are either hidden behind large seismic events, or do not have sufficient amplitude levels to rise above the average noise level on the two seismic arrays considered. We note that many winter storms never reach the north American coast, or turn further north into the Gulf of Alaska. A systematic analysis of storm characteristics in the north Pacific in relation to the "hum" is beyond the scope of this paper and will be addressed in a further study.

4. Comparison With Microseisms

[22] We have shown that infragravity waves generated by winter storms in the north Pacific Ocean contribute to the source of the low-frequency "hum" events observed in California and Japan.

[23] The nonlinear wave interactions that give rise to infragravity waves are also responsible for the generation of double-frequency microseisms [e.g., *Hasselmann*, 1962, 1963; *Longuet-Higgins*, 1950], which are themselves correlated with the wind wave spectrum [e.g., *Babcock et al.*, 1994; *Webb and Cox*, 1986; *Bromirski and Duennebier*, 2002], and are known to be generated primarily locally near the coast [e.g., *Haubrich and McCamy*, 1969; *Webb*, 1998; *Bromirski et al.*, 2005].

[24] Therefore we next investigate the relationship between microseisms, ocean storms and the low-frequency "hum." Even though there are two types of microseisms, primary (at periods lower than 10 s) and secondary, or "double-frequency," at periods
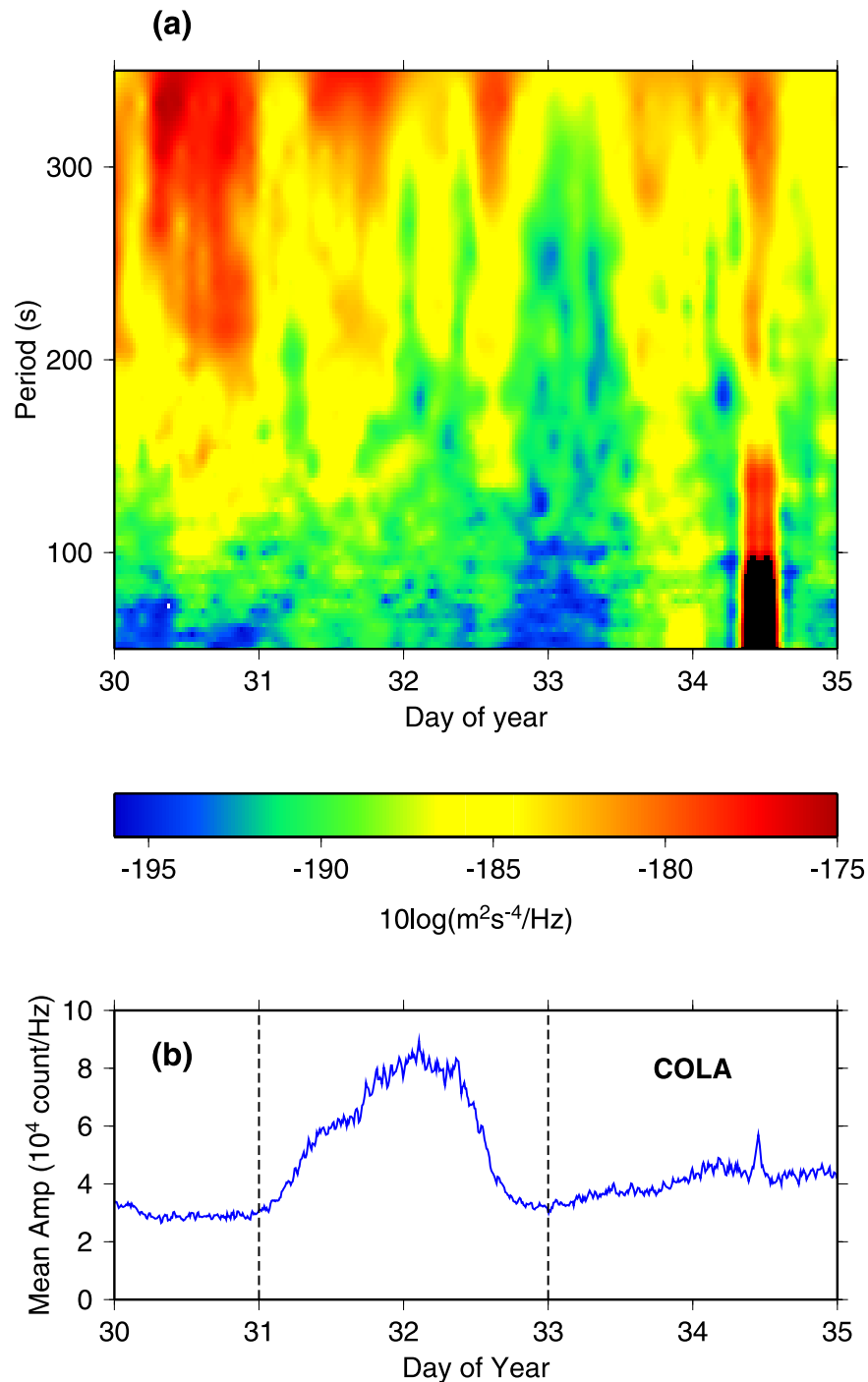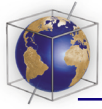
(a)

(b)

COLA

Figure 11. (a) Power spectral density (PSD) at COLA in Alaska. (b) Mean Fourier amplitude in the period range 2–25 s for COLA.

around 6–8 s [e.g., *Friedrich et al.*, 1998], and their generation mechanisms are different [e.g., *Hasselmann*, 1963; *Webb*, 1998], the double-frequency microseisms dominate the spectra and we will only consider those in the discussion that follows.

[25] We first computed mean Fourier amplitudes in the microseismic period band (2 to 25 s) at individual stations of BDSN and F-net for the time interval 2000.031–2000.035. We used moving windows of duration 30 mn, shifted by 10 mn. We removed mean and trend before computing Fourier amplitudes. We then compared them to
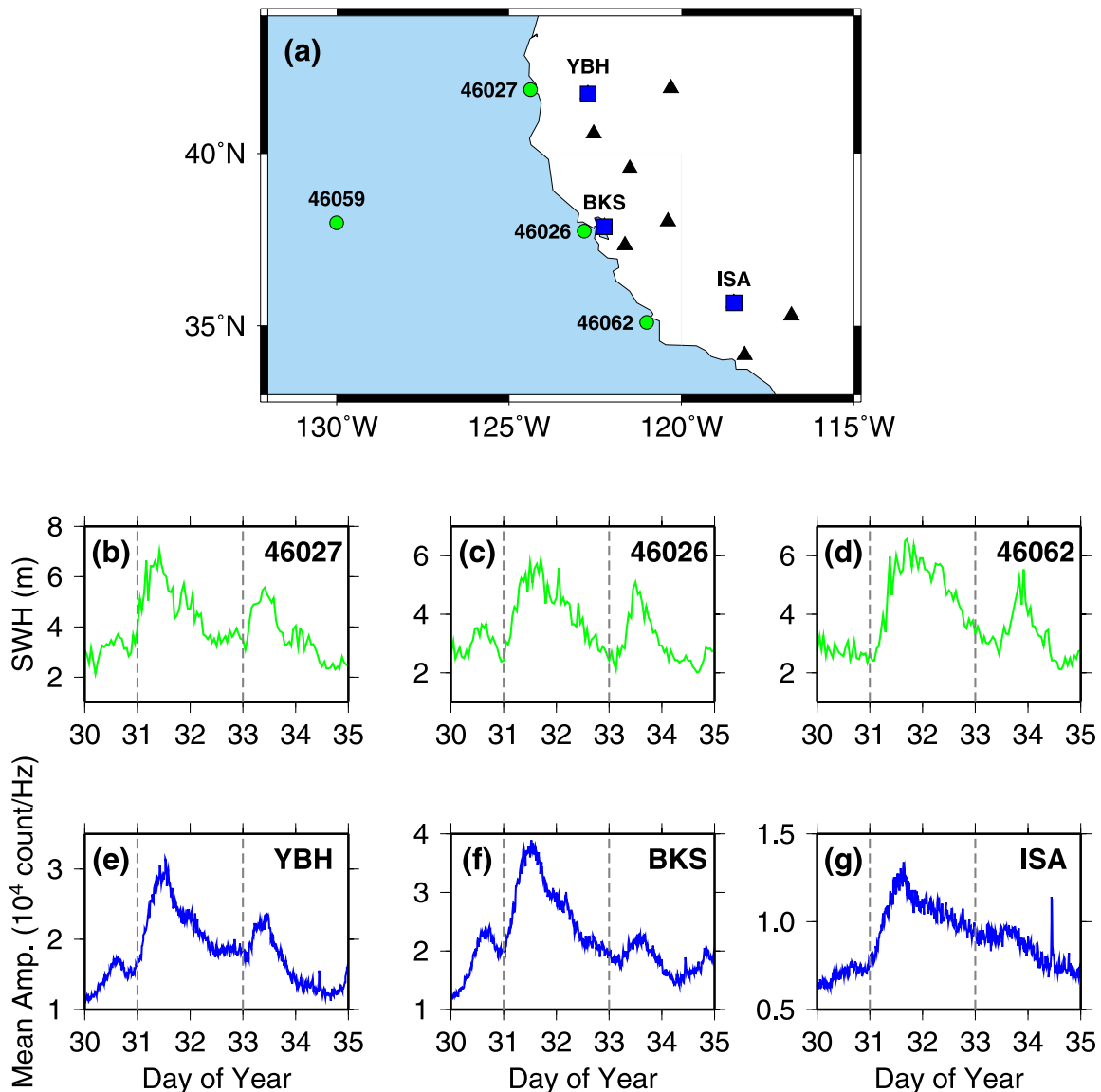
Figure 12. (a) Location map of BDSN and TerraScope stations (black triangle and blue squares) and buoys (green dots). Blue squares are seismic stations closest to the corresponding buoys. (b−d) Significant wave heights measured at buoy 46027, 46026, and 46052, respectively. (e−g) Mean Fourier amplitude (count/Hz) over the period range 2−25 s for YBH, BKS, and ISA.

near-by buoy data (Figures 12 and 13). Along the coast of California (Figure 12), the mean seismic amplitudes show the signatures of the two noise events already discussed at low frequency (on days 2000.031 and 2000.033), which are also well defined on the buoy data. The eastward moving storm arrives first in northern and central California, as seen by the slight delay in its wave height signature at buoy 46062 compared to the other two buoys (see also the data from buoy 46059 on Figure 7). The timing of the peak of microseismic noise at the three stations and the fact that the amplitude at station ISA is smaller by about a factor of 3 than at BKS, indicate that the generation of the microseisms occurs closer to the central and northern California buoys.

[26] Unfortunately, only data for three buoys are available around Japan for this time period. However, we note that the mean microseismic Fourier amplitudes at the three seismic broadband stations closest to the buoys show a good correlation with SWH data (Figure 13). We also note that, contrary to the observations in California, the timing and shape of the microseismic amplitude variations is different from that at "hum" frequencies, and
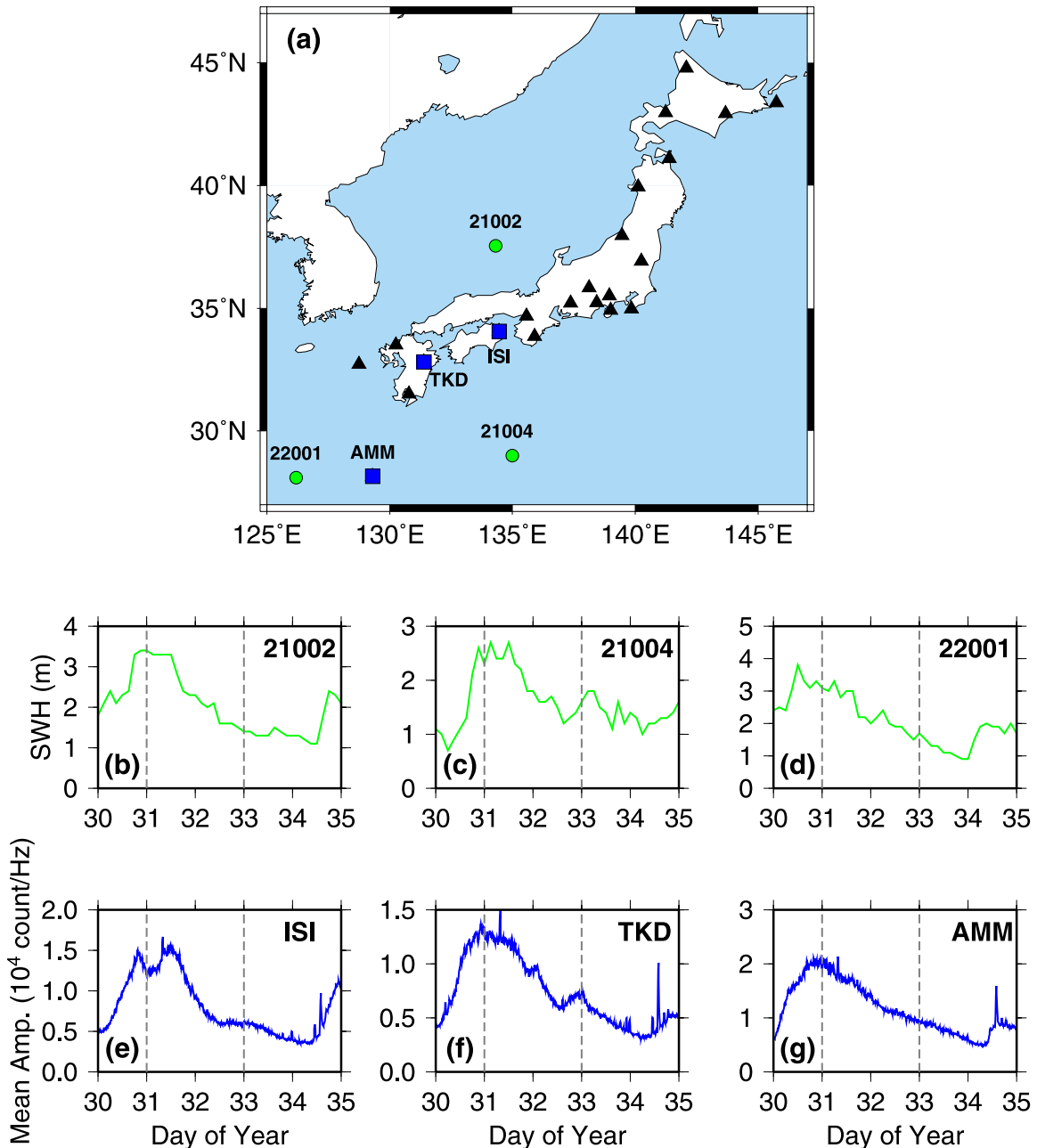
Figure 13. (a) Same as Figure 12 for F-net. (b−d) Same as Figures 12b, 12c, and 12d for 21002, 21004, and 22001, respectively. (e−g) Same as Figures 12e, 12f, and 12g for ISI, TKD, and AMM.

varies significantly with location of the station in the array (Figure 14), indicating that, in Japan, the sources of the microseismic noise and of the hum are distinct: the low-frequency noise is related to that observed on the eastern side of the Pacific (with a delay which we attribute to the propagation of infragravity waves across part of the Pacific Ocean), whereas the microseismic noise maximum occurs significantly earlier (on day 2000.030). In fact, the time histories of microseism energy at

stations within Japan differ and presumably depend on the location of each site relative to each storm track.

[27] To further investigate the relation between microseismic noise and the low-frequency hum, we need to be able to compare amplitude levels in the two frequency bands for long time intervals (e.g., a whole year). To do so effectively, we developed a data processing method that avoids
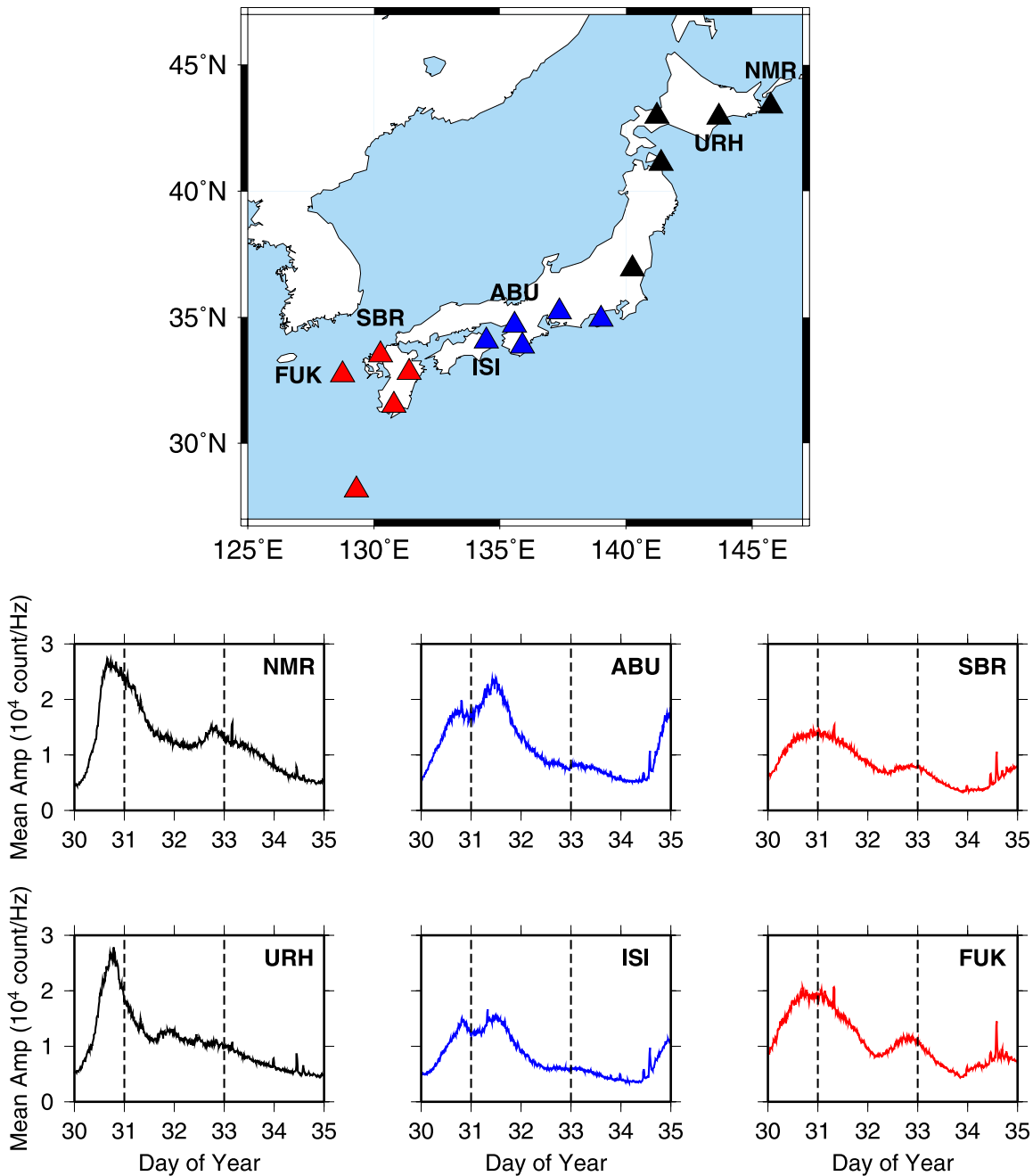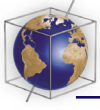
Figure 14. (top) Location map of seismic stations grouped by their locations in F-net. Different colors indicate different grouping. (bottom) Mean Fourier amplitude (count/Hz) over the period range 2−25 s for two selected stations in each group shown on the map at the top in black (left column), in blue (center column), and in red (right column). The variations in amplitude for all five stations (three of them are not shown) in the same group show similar overall trends.

eliminating the numerous time windows that are contaminated by earthquakes.

[28] Removing the effect of earthquakes at low frequencies is difficult to do precisely, due to the presence of lateral heterogeneity in the Earth and

the relatively low attenuation. In order to minimize their effects, we compute the minimum value, as a function of time, in a sliding 1.5 day interval, of the scaled MSA time series, using a moving time window with a 6 hour shift. This effectively removes some large amplitude peaks due to earth-
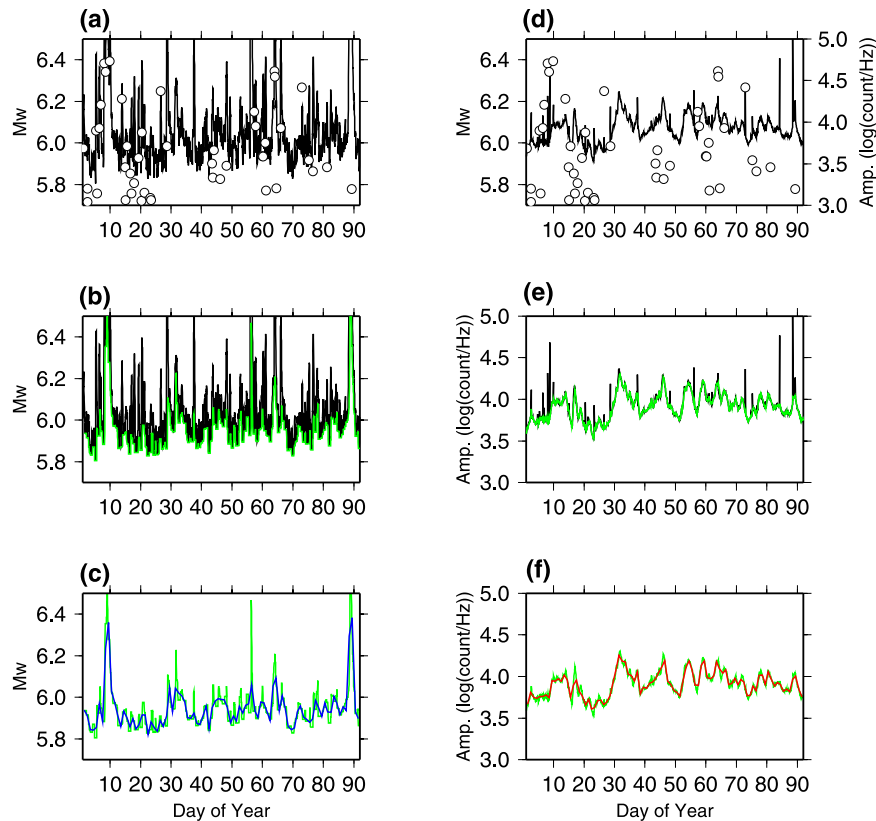
Figure 15. (a) Scaled long-period MSA, Gaussian filtered with center period of 240 s (black curves) for BDSN. Circles indicate earthquakes. (b) Black curve: same as in Figure 15a. Green curve: minimum obtained after applying moving time window with duration of 1.5 days and 6 hour shift. (c) Green curve: same as in Figure 15b. Blue curve: after low-pass filtering with corner period of 1 day. (d) Mean Fourier amplitude over the microseismic band (2–25 s) averaged over 7 BDSN stations (black curve). Dots are earthquakes as in Figure 15a. (e) Black curve: same as in Figure 15d. Green curve: after removing large gradient peaks. (f) Green curve: same as in Figure 15e. Red curve: low-pass filtered with corner period of 1 day.

quakes, but not all. We then apply a low-pass filter with a corner period of 1 day to the time series obtained in the previous step. This further removes most of the earthquake-related peaks, except for those with the longest duration, corresponding to the largest earthquakes (Figures 15a, 15b, and 15c). We also compute the mean Fourier amplitude in the microseismic band (2–25 s) for seven BDSN stations. Here the contamination by large earthquakes is not as severe and we only remove those points which correspond to large temporal gradients. To do so, we empirically determined a gradient threshold between two consecutive points in the amplitude time series: if the measured gradient is higher than the threshold, we remove the end point and test the gradient value for successive end points, until the gradient drops below the threshold. Finally, we low-pass filter the amplitude time series with a corner period of

1 day (Figures 15d, 15e, and 15f). This effectively removes most of the earthquake signals.

[29] We compare the filtered "hum" and microseism amplitude time series over a period of one year, for each array. In the case of California (BDSN), the level of low-frequency noise does not vary systematically with time (Figure 16a), but there is a seasonal variation in the microseismic amplitude, with a minimum during northern hemisphere summer time, as is also seen in the ocean wave height data (Figure 16b). This indicates that the sources of energy for the long-period and short-period noise are different during the summer. The variation in microseismic amplitude at BDSN stations is clearly related with ocean wave height measured by local buoys (Figure 16b). We can see a similar trend for F-net, but the correlation of the variation in short-period amplitudes and ocean
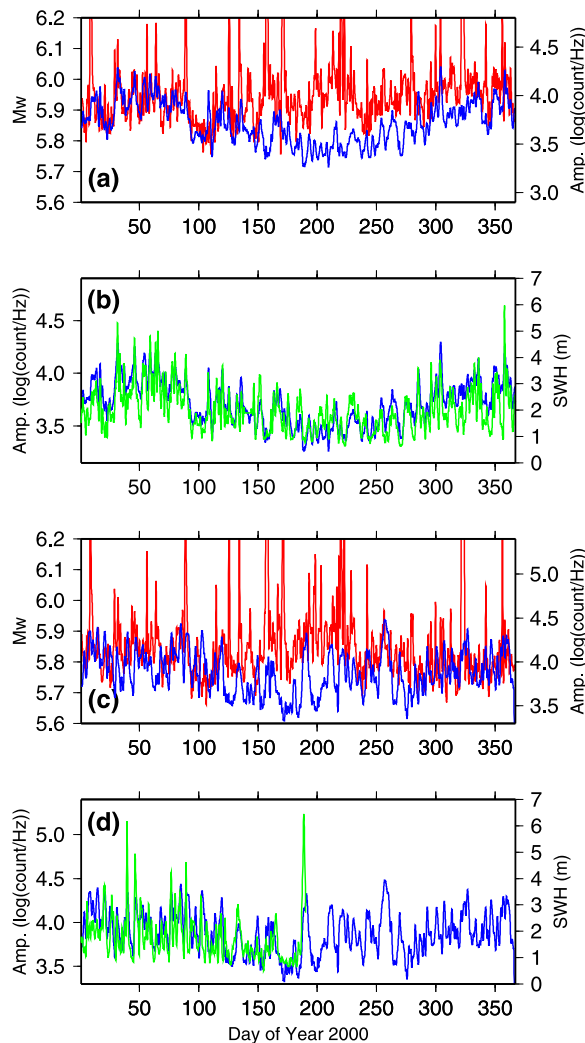
Figure 16. (a) Scaled long-period MSA (red) and short-period Fourier amplitude (blue), preprocessed as shown in Figure 15, for BDSN. The short-period mean Fourier amplitude was computed from 7 BDSN stations (BKS, CMB, MHC, MOD, ORV, WDC, and YBH). (b) Preprocessed short-period mean Fourier amplitudes (blue) for BDSN and significant wave height measured at buoy 46026 (green). The correlation coefficient between the two curves is 0.81. (c) Same as Figure 16a for 5 F-net stations near the eastern coast of Japan (AMM, ISI, NMR, TKD, and TMR). (d) Same as Figure 16b for F-net. Significant wave height data measured at buoy 21004 (green) is not available after day 190 in 2000. Large peaks in short-period mean Fourier amplitude and ocean waves during summer may be coming from the typhoon. The correlation coefficient between the two curves for the first part of the year is 0.58.

wave data is weaker than in the case of BDSN (Figures 16c and 16d).

[30] Removing the time periods contaminated by the largest events, and restricting our analysis to northern hemisphere winter (January to March and October to December), we compute the correlation coefficients between the low-frequency and high-frequency filtered noise time series, for three consecutive years, at BDSN. Correlation coefficients are significant, between 0.39 and 0.60 (Figure 17). This indicates that in the winter, both the low-frequency hum and the microseismic noise observed at BDSN are generated locally. On the other hand, the corresponding correlation coefficients for F-net are generally much lower: for the first 3 months of each year, respectively: −0.11, (N/A) and 0.21; for the last 3 months of each year, respectively: 0.22, −0.02, 0.30.

[31] The correlation between the hum and microseismic noise at BDSN during the winter is compatible with a common generation mechanism for both types of seismic noise, involving nonlinear interactions between surface ocean waves giving rise, on the one hand, to double-frequency microseisms, and on the other, to infragravity waves [e.g., *Hasselmann*, 1962]. The fact that the correlation is somewhat weaker at F-net is in agreement with our proposed scenario, in which the dominant effect is that of storms moving from West to East across the Pacific and reaching the west coast of North America to produce low-frequency seismic "hum."

5. Conclusions

[32] We have made progress in clarifying the mechanism of generation of continuous free oscillations, based on the observations for a time interval free of earthquakes during which two large long-period noise events are present in the MSA at BDSN and F-net. We have shown that these events can be related to a particular winter storm system.

[33] A perturbation in the atmosphere, typically a winter storm moving eastward across the north Pacific basin, generates short-period ocean waves. As the storm reaches the north-American coast, the nonlinear interaction between ocean waves generates long-period infragravity waves, some of which convert locally to long-period seismic energy, and others propagate long distance across the ocean basin and couple to the seafloor near northeastern coasts. The resulting long-period seismic waves propagate over the globe and give rise to the "hum." In particular, we were able to track the seismic energy generated off-shore California by the storm considered on day 2000.031, throughout the North American continent.
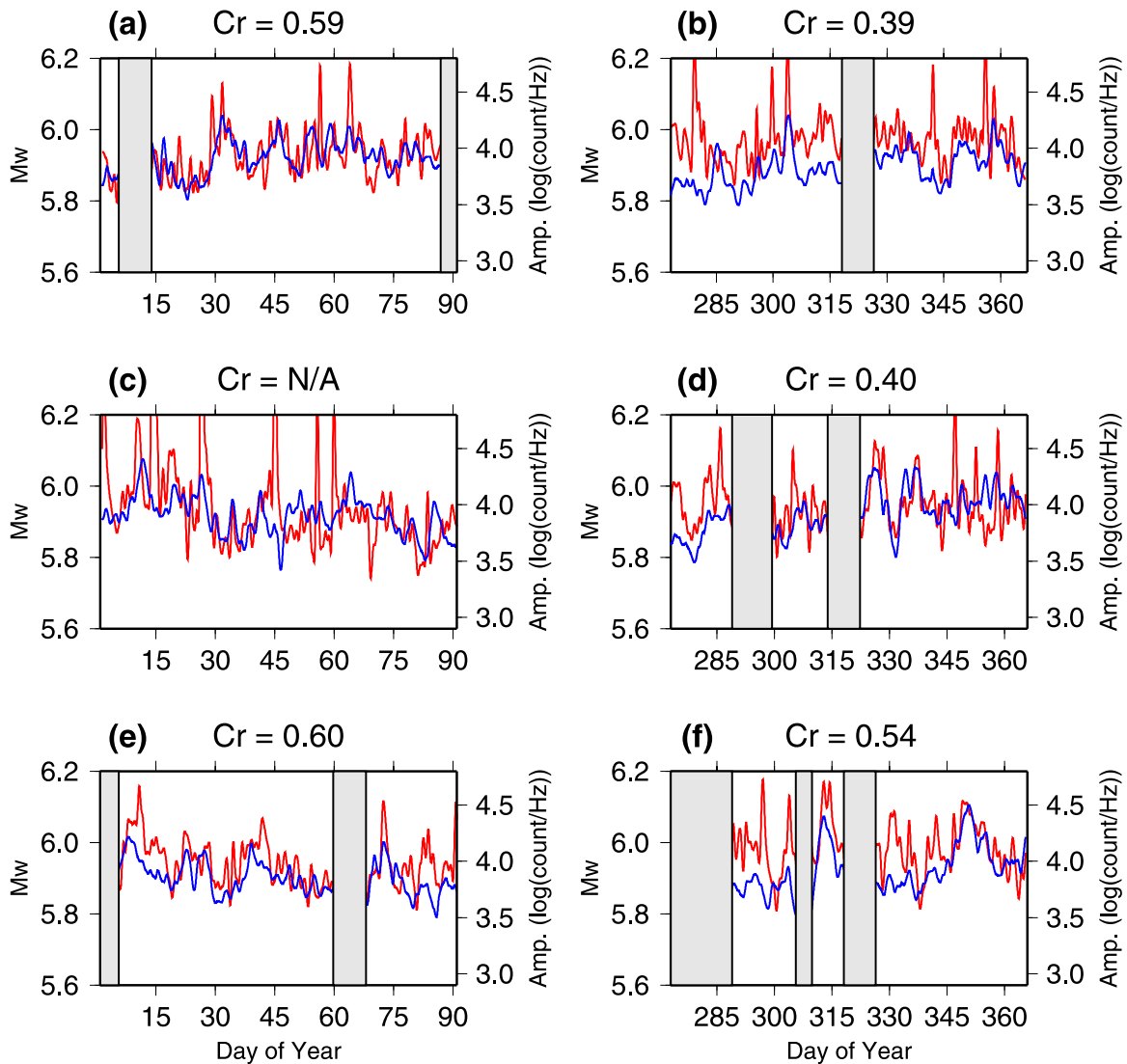
Figure 17. (a) Comparison between preprocessed scaled long-period MSA (red) and short-period mean Fourier amplitudes (blue) for the first three months of 2000. Time windows strongly contaminated by earthquakes are shaded in gray. Corresponding correlation coefficient is shown in the plot. (b) Same as Figure 17a for the last three months in 2000. (c–d) Same as Figures 17a and 17b for 2001. For Figure 17c, correlation coefficient is not computed because of significant contamination from earthquakes throughout the time period considered. (e–f) Same as Figures 17a and 17b for 2002.

[34] The directionality of the "hum" radiation suggested by our data needs to be further characterized, in particular for the benefit of studies of structure based on the analysis of noise cross-correlations [e.g., *Shapiro et al.*, 2005], at least at low frequencies. Indeed, the sources of low-frequency seismic noise can no longer be considered as uniformly distributed either in time, or in space.

[35] The annual fluctuations of long- (hum band) and short- (microseism band) period seismic amplitudes at BDSN and F-net show quite different

features. We can clearly see the seasonal change in amplitude in the microseism band (2–25 s) with a minimum during northern hemisphere summer, whereas the amplitude in the hum band (here considered at ∼240s) does not show clear seasonal variations. We also observed a significant correlation between seismic amplitudes at BDSN in the microseism and hum bands during northern hemisphere winter. We had previously documented that the source of the hum observed at BDSN and F-net shifts from the northern Pacific to the southern oceans between winter and summer, so that the
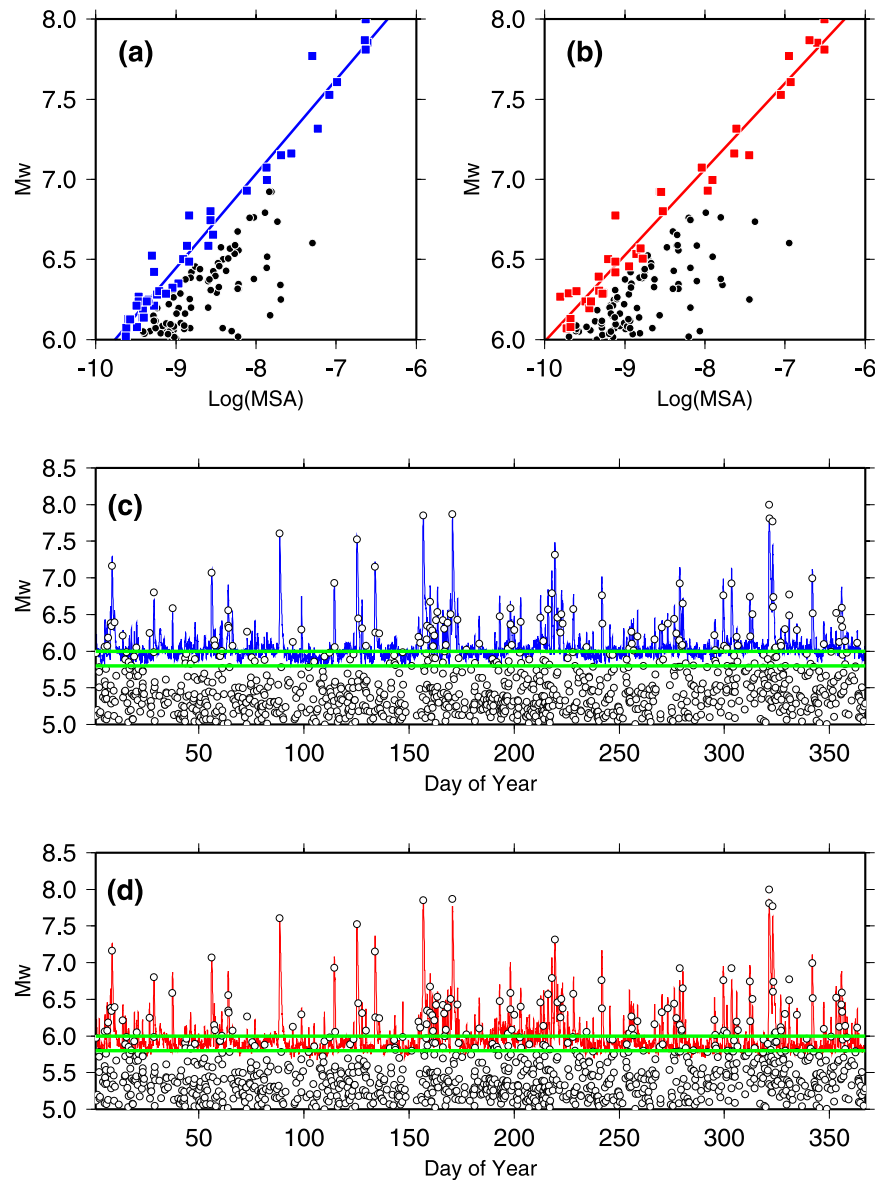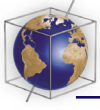
Figure A1. Estimation of the level of low-frequency background noise at ~240 s (i.e., the hum) for the year 2000. (a) Moment magnitudes versus associated maxima in MSA for BDSN. The MSA is shown after applying a moving average over a window of 6 hours with 1 hour offset. Results do not significantly change if no moving average is applied. Black dots indicate all seismic events during the year, and solid squares indicate selected maxima which are not contaminated by later Rayleigh wave trains from other large events. The best fitting line is computed using only the data indicated by blue squares. The best fitting line is used to scale MSA to match the plausible level of the back ground noise. (b) Same as Figure A1a for F-net. Red squares are selected maxima. (c) Scaled MSA (blue) for BDSN. Open circles represent all large events during the year 2000. The levels corresponding to M_w 5.75 and M_w 6 are highlighted with green lines. (d) Same as Figure A1c for F-net (red).

sources are more "local" in the winter than in the summer. In contrast, microseisms propagate less efficiently at large distances, so the source is primarily local. These observations are in agreement with a common mechanism for the simultaneous generation of short- and long-period seismic noise near the California coast, as inferred from theoretical studies.

Appendix A

[36] We estimate the background level of the low-frequency seismic energy by determining a scaling

factor between the observed peak amplitudes (from the MSA at 240 s), and the moment magnitudes of the corresponding earthquakes ($M_w > 6.0$), as listed in the Harvard CMT catalog [*Dziewonski and Woodhouse*, 1983].

[37] Since we know the location of both the array and each earthquake, as well as the event origin time, we can calculate the theoretical onset time of the R1 train at the center of the array and select only those peaks that correspond to the arrival time of the R1 train. However, the selection of R1 peaks is made difficult by the presence of secondary peaks corresponding to later arriving Rayleigh wave trains from the previous larger earthquakes (R2,R3...). When such secondary peaks are present, the corresponding seismic amplitude is significantly larger than estimated, on average, based on the magnitude of the earthquake considered. When estimating the scaling factor, and to reduce contamination due to large previous events, we therefore discard those peaks from the data set that have relatively high amplitude for a given magnitude level. This means that, when applying this scaling factor, our estimate of the hum level is maximum (Figures A1a and A1b). Since we ignore the effects of geometrical spreading, attenuation during propagation, as well as radiation pattern, this is a very crude estimate. However, the estimated noise background level is consistent with what has been previously reported (Figures A1c and A1d) from the analysis of free oscillation data (e.g., M_w 5.75 [*Ekström*, 2001]; M 6.0 [*Tanimoto and Um*, 1999]).

Acknowledgments

References

Babcock, J. M., B. A. Kirkendall, and J. A. Orcutt (1994), Relationships between ocean bottom noise and the environment, *Bull. Seismol. Soc. Am.*, *84*, 1991–2007.

Bromirski, P. D., and F. K. Duennebier (2002), The near-coastal microseism spectrum: Spatial and temporal wave climate relationships, *J. Geophys. Res.*, *107*(B8), 2166, doi:10.1029/2001JB000265.

Bromirski, P. D., F. Duennebier, and R. A. Stephen (2005), Mid-ocean microseisms, *Geochem. Geophys. Geosyst.*, *6*, Q04009, doi:10.1029/2004GC000768.

Dolenc, D., B. Romanowicz, D. Stakes, P. McGill, and D. Neuhauser (2005a), Observations of infragravity waves at

the Monterey ocean bottom broadband station (MOBB), *Geochem. Geophys. Geosyst.*, *6*, Q09002, doi:10.1029/2005GC000988.

Dolenc, D., B. Romanowicz, D. Stakes, P. McGill, and D. Neuhauser (2005b), Observations of infragravity waves at the Monterey ocean bottom broadband station (MOBB), *Eos Trans. AGU*, *85*(52), Fall Meet. Suppl., Abstract S34B-05.

Dziewonski, A. M., and D. L. Anderson (1981), Preliminary reference Earth model, *Phys. Earth Planet. Inter.*, *25*, 297–356.

Dziewonski, A. M., and J. H. Woodhouse (1983), Studies of the seismic source using normal-mode theory, in *Earthquakes: Observation, Theory, and Interpretation: Notes From the International School of Physics "Enrico Fermi" (1982: Varenna, Italy)*, edited by H. Kanamori and E. Boschi, pp. 45–137, Elsevier, New York.

Ekström, G. (2001), Time domain analysis of Earth's long-period background seismic radiation, *J. Geophys. Res.*, *106*, 26,483–26,493.

Ekström, G., and S. Ekström (2005), Correlation of Earth's long-period background seismic radiation with the height of ocean waves, *Eos Trans. AGU*, *86*(52), Fall Meet. Suppl., Abstract S34B-02.

Elgar, S., T. H. C. Herbers, M. Okihiro, J. Oltman-Shay, and R. T. Guza (1992), Observations of infragravity waves, *J. Geophys. Res.*, *97*, 15,573–15,577.

Friedrich, A., F. Krüger, and K. Klinge (1998), Ocean-generated microseismic noise located with the Gräfenberg array, *J. Seismol.*, *2*, 47–64.

Hasselmann, K. (1962), On the non-linear energy transfer in a gravity-wave spectrum, Part I. General theory, *J. Fluid Mech.*, *12*, 481–500.

Hasselmann, K. (1963), A statistical analysis of the generation of microseisms, *Rev. Geophys.*, *1*, 177–210.

Haubrich, R. A., and K. McCamy (1969), Microseisms: Coastal and pelagic sources, *Rev. Geophys.*, *7*, 539–571.

Herbers, T. H. C., S. Elgar, and R. T. Guza (1994), Infragravity-frequency (0.005–0.05 Hz) motions on the shelf, Part I: Forced waves, *J. Phys. Oceanogr.*, *24*, 917–927.

Herbers, T. H. C., S. Elgar, and R. T. Guza (1995a), Generation and propagation of infragravity waves, *J. Geophys. Res.*, *100*, 24,863–24,872.

Herbers, T. H. C., S. Elgar, R. T. Guza, and W. C. O. Reilly (1995b), Infragravity-frequency (0.005 0.05 Hz) motions on the shelf, Part II: Free waves, *J. Phys. Oceanogr.*, *25*, 1063–1079.

Longuet-Higgins, M. S. (1950), A theory of the origin of microseisms, *Philos. Trans. R. Soc. London, Ser. A*, *243*, 1–35.

Longuet-Higgins, M. S., and R. W. Stewart (1962), Radiation stress and mass transport in surface gravity waves with application to "surf beats," *J. Fluid Mech.*, *13*, 481–504.

Munk, W. (1949), Surf beats, *Eos Trans. AGU*, *30*, 849–854.

Munk, W., F. Snodgrass, and F. Gilbert (1964), Long waves on the continental shelf: An experiment to separate trapped and leaking modes, *J. Fluid Mech.*, *20*, 529–554.

Nawa, K., N. Suda, Y. Fukao, T. Sato, Y. Aoyama, and K. Shibuya (1998), Incessant excitation of the Earth's free oscillations, *Earth Planets Space*, *50*, 3–8.

Nishida, K., and Y. Fukao (2004), Spatial variations of excitation amplitudes of Earth's background free oscillations, *Eos Trans. AGU*, *84*(46), Fall Meet. Suppl., Abstract S31B-1068.

Nishida, K., and N. Kobayashi (1999), Statistical features of Earth's continuous free oscillations, *J. Geophys. Res.*, *104*, 28,731–28,750.

Nishida, K., N. Kobayashi, and Y. Fukao (2000), Resonant oscillations between the solid Earth and the atmosphere, *Science*, *287*, 2244–2246.

Okihiro, M., R. T. Guza, and R. J. Seymour (1992), Bound infragravity waves, *J. Geophys. Res.*, *97*, 11,453–11,469.

Rhie, J., and B. Romanowicz (2003), Detection and location of long period surface wave energy sources, *Eos Trans. AGU*, *84*(46), Fall Meet. Suppl., Abstract S42E-0211.

Rhie, J., and B. Romanowicz (2004), Excitation of Earth's continuous free oscillations by atmosphere-ocean-seafloor coupling, *Nature*, *431*, 552–556.

Roult, G., and W. Crawford (2000), Analysis of 'background' free oscillations and how to improve resolution by subtracting the atmospheric pressure signal, *Phys. Earth Planet. Inter.*, *121*, 325–338.

Shapiro, N. M., M. Campillo, L. Stehly, and M. H. Ritzwoller (2005), High-resolution surface-wave tomography from ambient seismic noise, *Science*, *307*, 1615–1618.

Suda, N., K. Nawa, and Y. Fukao (1998), Earth's background free oscillations, *Science*, *279*, 2089–2091.

Sutton, G. H., W. G. McDonald, D. D. Prentiss, and S. N. Thanos (1965), Ocean-bottom seismic observatories, *Proc. IEEE*, *53*, 1909–1921.

Tanimoto, T. (2003), Jet stream, roaring ocean waves, and ringing Earth, *Eos Trans. AGU*, *84*(46), Fall Meet. Suppl., Abstract S12F-04.

Tanimoto, T. (2005), The oceanic excitation hypothesis for the continuous oscillations of the Earth, *Geophys. J. Int.*, *160*, 276–288.

Tanimoto, T., and J. Um (1999), Cause of continuous oscillations of the Earth, *J. Geophys. Res.*, *104*, 28,723–28,739.

Tolman, H. L. (1999), User manual and system documentation of WAVEWATCH III, version 1.18, *Tech. Rep. Ocean Modeling Branch Contrib. 166*, NOAA/NWS/NCEP, Silver Spring, Md.

Tucker, M. J. (1950), Surf beats: Sea waves of 1 to 5 min period, *Proc. R. Soc. London, Ser. A*, *207*, 565–573.

Watada, S., and G. Masters (2001), Oceanic excitation of the continuous oscillations of the Earth, *Eos Trans. AGU*, *82*(47), Fall Meet. Suppl., Abstract S32A-0620.

Webb, S. (1998), Broadband seismology and noise under the ocean, *Rev. Geophys.*, *36*, 105–142.

Webb, S. C., and C. S. Cox (1986), Observations and modeling of seafloor microseisms, *J. Geophys. Res.*, *91*, 7343–7358.

Webb, S., X. Zhang, and W. Crawford (1991), Infragravity waves in the deep ocean, *J. Geophys. Res.*, *96*, 2723–2736.

Wielandt, E., and J. M. Steim (1986), A digital very-broadband seismograph, *Ann. Geophys., Ser. B*, *4*, 227–232.

Wielandt, E., and G. Streckeisen (1982), The leaf-spring seismometer: Design and performance, *Bull. Seismol. Soc. Am.*, *72*, 2349–2367.